Full length article

Slip transmission assisted by Shockley partials across α/β interfaces in Ti-alloys

Pengyang Zhao [a], Chen Shen [b], Michael F. Savage [c], Ju Li [d], Stephen R. Niezgoda [a], Michael J. Mills [a], Yunzhi Wang [a, *]

[a] Department of Materials Science and Engineering, The Ohio State University, 2041 College Road, Columbus, OH, 43210, USA
[b] GE Global Research, One Research Circle, Niskayuna, NY, 12309, USA
[c] ASSA ABLOY Americas, 110 Sargent Dr, New Haven, CT, 06511, USA
[d] Department of Nuclear Science and Engineering and Department of Materials Science and Engineering, Massachusetts Institute of Technology, 77 Massachusetts Avenue, Cambridge, MA, 02139, USA

ARTICLE INFO

ABSTRACT

Slip transmission across α/β interfaces is of great significance in understanding the strength of Ti-alloys, but currently a detailed mechanistic understanding of the process is still lacking. Here we develop a microscopic phase-field framework that incorporates the generalized stacking fault energy and the interface crystallography, which are, respectively, calculated by atomistic methods and revealed by crystallographic theories of phase transformations and experimental characterization. The model is then applied to studying the transmission of a constant flux of discrete dislocations across multiple α/β interfaces at micron-scale. The simulations predict interesting slip transmission mechanisms that have not been reported before, wherein Shockley partials play a critical role in assisting the dislocation transfer across the interfaces. The dislocation configurations generated by these mechanisms seem to agree well with experimental characterizations. Spatial cross-over between full dislocations in α is also seen from the simulations, which is again attributed to a reaction mechanism involving Shockley partials. A parametric study further reveals that stacking fault energy can influence the slip transmission in terms of transmitted dislocation types, transmission rate, and the residual dislocation content, suggesting a new strengthening strategy at the α/β interface level. This work offers new understanding of the complex slip transmission process in Ti-alloys and demonstrates a new computational tool complementary to advanced electron microscopy analysis of plastic deformation.

© 2019 Acta Materialia Inc. Published by Elsevier Ltd. All rights reserved.

1. Introduction

Titanium alloys are widely used in aerospace and energy applications owing to their high specific strength, high modulus and good toughness, and high service temperature. The strength of Ti-alloys can be further engineered and optimized for specific purposes via different thermomechanical processing routes, which lead to a wide variety of microstructures containing differently distributed α and β phases. The resulting hierarchy of structural heterogeneities such as prior β grain boundaries, α colony boundaries, and α/β interfaces are expected to control the alloys' mechanical properties such as room temperature creep, yield strength,

and strain hardening [1–3]. For example, deformation characterizations have revealed that dislocation transfer across the α/β interfaces, i.e., the so-called *slip transmission*, can be highly anisotropic for different slip systems, which is considered to be the primary reason for the observed anisotropic deformation properties such as yield strength and hardening rate [2,3]. However, the mechanistic understanding of slip transmission across α/β interfaces (and across a general metal-metal interface) is still largely missing [4,5].

In general, slip transmission across interfaces in metals is of critical importance to a class of unsolved issues, for instance, some emergent observations such as twinning in bimetal nanocomposites [6,7], the strength of multilayers [8,9], and even some long-standing topics such as plasticity of polycrystals and precipitation-hardened alloys. It is expected that interfaces (including both grain boundaries and heterophase interfaces) can

---

* Corresponding author.
E-mail address: wang.363@osu.edu (Y. Wang).

act as barriers to the propagation of dislocation glide. Studies utilizing experimental measurement and characterization together with continuum dislocation theory have proposed different transmissibility criteria based on either geometrical factors [10–14] or stress factors [15–17], or the combination of both [18]. Efforts from atomistic simulations [19–22] have revealed the interplay between the atomic structures of the transmitting dislocation core and the interface, which is ignored in the continuum criteria but may exhibit some macroscopic effects. Recently, a model [23] based on phase-field (PF) dislocation dynamics [24–26] has been applied to calculate the critical stress required for a perfect dislocation transmitting a cube-on-cube interface, presenting a mesoscale modeling approach of slip transmission.

To date, modeling efforts at multiple scales have been made, aiming at a full-scale understanding of slip transmission. Nevertheless, these existing works focus mainly on the features of an individual dislocation transfer event; the transmission of a flux of dislocations, which involves not only the dislocation-interface interaction but also the interaction between dislocations and residual dislocations deposited at the interface, has been largely ignored. In addition, the representative volume element (RVE) considered so far contains only a single interface; such RVE suffices to the study of cases such as conventional polycrystals where the transmitted dislocation will most likely interact with an obstacle inside the (large enough) grain before it arrives at the next interface (grain boundary), but may not be suitable for the study of nano-structured materials where the distance between adjacent interfaces is comparable to the mean free path of dislocations. The latter implies particular requirement for choosing RVE when studying slip transmission of a dislocation flux.

To study the underlying mechanisms during slip transmission across α/β interfaces in Ti-alloys, we adopt a microscopic phase-field framework [27], utilize the generalized stacking fault energy surface and the elastic stiffness constants obtained by atomistic calculations, and incorporate the interface crystallography revealed by experimental characterizations. The developed model is then applied to simulating the transmission of a constant flux of discrete dislocations across multiple α/β interfaces in a representative volume element (RVE) of single colony Ti-alloys. The rest of the paper is organized as the following. Section 2 presents the methodology, model input, and simulation setup. Simulation results of slip transmission with detailed dislocation transfer processes are shown in Section 3. The underlying slip transmission mechanisms and the subsequent implication on understanding the microstructure-property relationship in Ti-alloys are discussed in Section 4, with major findings being summarized in Section 5. The current work also demonstrates a new physics-based computational framework of studying the interface-dislocation interactions at the mesoscale over a few interface-interface distances, which is currently missing in the literature.

2. Methodology

2.1. Microscopic phase-field

To study slip transmission across interfaces via dislocation glide, descriptions of the dislocation and interface are needed. We adopt the *microscopic phase-field* (MPF) model developed by Shen, Li, and Wang [27,28], which allows the consideration of arbitrary dislocation or dislocation network configurations and offers the equilibrium structure of the dislocation core or network configurations as the complete model prediction. The incorporation of the generalized stacking fault (GSF) energy surface (or the γ-surface) and the

elastic stiffness constants obtained by atomistic calculations, together with the removal of the gradient term in the energy formulation at the sub-atomic scale, enables MPF to accurately describe the structure of dislocations in a generalized manner of the classical Peierls model [29]. The model has recently been applied to studying the grain boundary structures in BCC metals by Qiu et al. [30]. In the following, we present the key equations in the model and more details can be found in Refs. [27,30].

In MPF model, the total free energy is a functional parameterized by a set of N order parameters, $\left\{\eta_p(\mathbf{x})\right\}_{p=1}^{N}$ ($\mathbf{x}$ is the position vector in real space), which characterize the so-called disregistry associated with a set of Burgers vectors (or more generally the basis displacement vectors [30]), $\left\{\mathbf{b}_p\right\}_{p=1}^{N}$, as defined in the Peierls model. In our current MPF model for a two-phase system, an eigenstrain (under small strain assumption) is associated with each Burgers vector and defined as

$$\boldsymbol{\varepsilon}_p^{\mathrm{s}} = \frac{\mathbf{b}_p^{\mathrm{s}} \otimes \mathbf{n}_p^{\mathrm{s}} + \mathbf{n}_p^{\mathrm{s}} \otimes \mathbf{b}_p^{\mathrm{s}}}{2d}, \quad \mathrm{s} = \alpha \text{ or } \beta, \tag{1}$$

where the superscript s indicates the phase type and $\mathbf{n}_p^{\mathrm{s}}$ is the slip plane normal and d is the interplanar spacing of the slip plane (assumed to be the same for all planes in question). The resulting total displacement $\mathbf{u}(\mathbf{x})$ is given as

$$\mathbf{u}(\mathbf{x}) = \sum_{\mathrm{s}} \sum_{p=1}^{N^{\mathrm{s}}} \eta_p^{\mathrm{s}}(\mathbf{x})\mathbf{b}_p^{\mathrm{s}}. \tag{2}$$

In a recent paper by Qiu et al. [30], it has been shown that arbitrary basis displacement vectors (i.e., $\mathbf{b}_p^{\alpha}$ and $\mathbf{b}_p^{\beta}$ in Eq. (2)) can be chosen as long as they are non-collinear. Consequently, we set $N^{\alpha} = N^{\beta} = N = 2$ and use two orthogonal vectors for both α and β phases in the simulation. Following the spirit of the Peierls model, $\mathbf{u}(\mathbf{x})$ is assumed to be inelastic and confined in the slip plane of dislocations, leading to a so-called crystalline energy E^{m}.

$$E^{\mathrm{m}} = \int \Big(\phi(\mathbf{x})\gamma^{\alpha}[\mathbf{u}(\mathbf{x})] + (1 - \phi(\mathbf{x}))\gamma^{\beta}[\mathbf{u}(\mathbf{x})]\Big)dA \tag{3}$$

where $\phi(\mathbf{x})$ is a field describing the local phase identity, namely,

$$\phi(\mathbf{x}) = \begin{cases} 1, & \text{if } \mathbf{x} \in \alpha \\ 0. & \text{if } \mathbf{x} \in \beta \end{cases} \tag{4}$$

For the current purpose, the microstructure $\phi(\mathbf{x})$ is predefined by choosing the appropriate RVE and kept static during the slip transmission simulation, but may need to be evolved for cases such as high-temperature deformation where concurrent evolution of microstructure and micromechanics are involved [31–33]. In Eq. (3) γ^{α} and γ^{β} are the γ-surface of α and β phases, respectively, which depend on $\mathbf{u}(\mathbf{x})$, and the integral is over the slip plane. The *localized* crystalline energy will cause elastic distortions in the rest of the bulk crystal (other than the slip plane), which result in the elastic strain energy E^{el}. The closed-form of E^{el} follows the phase-field microelasticity theory [34] and is given as

$$E^{\mathrm{el}} = \frac{1}{2}\sum_{\mathrm{s}}\sum_{p,q}^{N} \iint \left[\Lambda_{pq}^{\mathrm{s}}(k_x, k_y)\tilde{\eta}_p^{\mathrm{s}}(k_x, k_y)\tilde{\eta}_q^{\mathrm{s*}}(k_x, k_y)\right]\frac{dk_xdk_y}{(2\pi)^2},$$

$$\tag{5}$$

$$\Lambda_{pq}^{s}(k_x, k_y) = d^2 \int \left[C_{ijkl} \varepsilon_{pij}^{s} \varepsilon_{qkl}^{s} - \hat{k}_i \sigma_{pij}^{s} \Omega_{jk}\left(\hat{\mathbf{k}}\right) \sigma_{qkl}^{s} \hat{k}_l \right] \frac{dk_z}{(2\pi)},$$
$$s = \alpha \text{ or } \beta,$$

(6)

where k_x and k_y are components of the reciprocal vector $\mathbf{k}$, $\hat{\mathbf{k}} = \frac{\mathbf{k}}{|\mathbf{k}|}$ is the corresponding unit vector, $\tilde{\eta}_p^{s}$ is the Fourier transform of η_p^{s} and $\tilde{\eta}_p^{s*}$ is its complex conjugate, C_{ijkl} is the elastic stiffness tensor, $\sigma_{pij}^{s} \equiv C_{ijkl} \varepsilon_{pkl}^{s}$, and Ω_{jk} is specified by defining its inverse as $\Omega_{jk}^{-1} \equiv C_{ijkl} \hat{k}_i \hat{k}_l$. Eqs. (5) and (6) provide a general solution to the elastic energy (in 3D) associated with any arbitrary dislocation configurations at the mechanical equilibrium, and ensure high computational efficiency owing to the usage of the Green's function in the reciprocal space and the fast Fourier transform (FFT) algorithm during the numerical implementation. The total energy in MPF is given as

$$E^{\text{tot}} = E^{\text{m}} + E^{\text{el}} + W$$

(7)

where, apart from the previous crystalline and elastic energies, the term W is the work done by the external applied stress σ_{ij}^{a}:

$$W = -\int \sigma_{ij}^{a} \varepsilon_{ij}^{\text{tr}}(\mathbf{x}) dV.$$

(8)

In Eq. (8), $\boldsymbol{\varepsilon}^{\text{tr}}(\mathbf{x}) = \sum_s \sum_p^N \eta_p^{s}(\mathbf{x}) \boldsymbol{\varepsilon}_p^{s}$ is the (actual) transformation strain field that is obtained from the linear coupling of the order parameter and eigenstrain tensor (Eq. (1)). Once the total energy E^{tot} is formulated solely as a functional of the order parameters, the subsequent dislocation dynamics is modeled by the linear dissipative law:

$$\frac{\partial \eta_p^{s}}{\partial t} = -L_p \frac{\delta E^{\text{tot}}}{\delta \eta_p^{s}}$$

(9)

where t is time and L_p is a constant coefficient controlling the dynamics rate. In the slip transmission simulation, the initially prescribed dislocation configuration will be driven by the external applied stress and the subsequent evolution of the order parameters will give the complete information about the process.

Note that in Eq. (7) there is no energy term associated with the gradient of the order parameters, which is, however, commonly present in some previous PF dislocation models [24–26]. The current MPF model is a 3D extension of the Peierls model [29] for dislocation core structure, which resides in the sub-atomic length scale and no gradient term is present in the original Peierls model [28]. From the energy perspective, the crystalline energy E^{m} (determined by the displacement fields and GSF energy surface) is a *local* contribution and competes with the *non-local* contribution due to the elastic strain energy E^{el} (depending on the gradient of the displacement, i.e., strain), leading to an equilibrium dislocation core structure.

2.2. Model input

2.2.1. Material properties of individual phases

MPF model requires only two sets of material properties as input, (i) GSF energy surface (on the slip plane) and (ii) elastic stiffness constants, both of which should be obtained consistently from one set of atomistic calculations. For α/β two-phase Ti-alloys, we need to consider first the material inputs for individual α and β phases. In the β phase (BCC crystal structure), one frequently observed

dislocation slip system on the $\{0\,\overline{1}\,1\}_\beta$ plane with the Burgers vector of $\frac{a_\beta}{2}\langle 1\,1\,1\rangle_\beta$ where a_β is the lattice parameter of β phase. In the α phase (HCP crystal structure), there are two major slip systems observed in experiments, i.e., the basal slip of $\frac{a_\alpha}{3}\langle 2\,\overline{1}\,\overline{1}\,0\rangle_\alpha/\{0\,0\,0\,1\}_\alpha$ and the prismatic slip of $\frac{a_\alpha}{3}\langle\overline{1}\,\overline{1}\,2\,0\rangle_\alpha/\{1\,\overline{1}\,0\,0\}_\alpha$. In our current work, we only consider the basal slip, whose role in slip transmission has been studied in a previous experimental work by Savage et al. [3].

Given the slip systems to be considered, the corresponding GSF energy surfaces on the slip planes ($\{0\,0\,0\,1\}_\alpha$ and $\{0\,\overline{1}\,1\}_\beta$) can be calculated using atomistic methods such as density functional theory (DFT) or molecular dynamics (MD). The GSF energy data to be used in this work are based on the empirical potential of Ti in Ref. [35] with additional correction from DFT calculation on some special points such as unstable stacking fault and intrinsic stacking fault (Li, J. Private Communication). Our DFT corrected GSF energy leads to a value of $290\,\text{mJ/m}^2$ for the intrinsic stacking fault energy, which is close to the experimental value of $\sim 300\,\text{mJ/m}^2$ [38]. The elastic constants are in principle different for the two phases; for simplicity, however, we take those of β phase ($c_{11} = 97.7\,\text{GPa}$, $c_{12} = 82.7\,\text{GPa}$, $c_{44} = 37.5\,\text{GPa}$) and assume a homogeneous elastic medium as a reasonable approximation discussed previously in Refs. [36,37,39].

2.2.2. Crystallographic orientation relationship between α and β

The two GSF energy surfaces need to be brought together to match the specific crystallographic orientation relationship (OR) between α and β in the given Ti-alloys. The Burgers OR:

$$(1\,0\,1)_\beta \,\big|\big|\, (0\,0\,0\,1)_\alpha, \quad \left[1\,\overline{1}\,\overline{1}\right]_\beta \,\big|\big|\, \left[2\,\overline{1}\,\overline{1}\,0\right]_\alpha$$

(10)

has been well observed between laths of α and β phase in the Widmanstätten colonies of many Ti-alloys. In addition, small deviations (rotation of $\sim 1°$ about the $[1\,0\,1]_\beta \,\big|\big|\, [0\,0\,0\,1]_\alpha$ direction) from Eq. (10), the so-called near-Burgers ORs, have also been observed in some Ti-alloys [2,3,40]. For the purpose of comparison with the relevant experiment, we adopt the near-Burgers OR observed by Savage et al. [3] in a commercial α/β Ti-alloy (Ti-6Al-2Sn-4Zr-2Mo-0.1Si, Ti6242, in weight percent), as shown in Fig. 1a. By matching the individual GSF energy surfaces of α and β to this near Burgers OR, we obtain the combined GSF energy surface for the coplanar slip plane $(1\,0\,1)_\beta \,\big|\big|\, (0\,0\,0\,1)_\alpha$ as shown in Fig. 1b. Note that we have ignored the possible effect of solutes on GSF energy due to their small amounts in the alloy considered. One may also note that a displacement of $\frac{2}{3}a_\alpha\left[0\,\overline{1}\,1\,0\right]_\alpha$ leads to a local minimum, which is also seen in a previous first-principle calculation [41].

2.2.3. Simulation setup

In accordance with the near-Burger OR as illustrated and also revealed by the bright-field TEM image in Fig. 1a for Ti6242 [3], we set up a RVE to describe the α/β two-phase microstructure of interest. As a first modeling effort tackling the slip transmission across the α/β interface, we focus on the transmission of straight **a**-type dislocations across a flat and sharp α/β interface that is assumed to be coherent, leaving the effects of the interface defects such as structural ledges [2,40] to the future work. This simplified scenario allows us to take part of the real α/β interface (as, for example, denoted by the dashed rectangle in Fig. 1a) and set up the model interface on $(1\,0\,1)_\beta \,\big|\big|\, (0\,0\,0\,1)_\alpha$ as illustrated in Fig. 1a.

In addition, dislocations undergoing slip transmission will exhibit certain line configurations as revealed by the TEM characterizations in Ref. [3], which is closely related to the type of
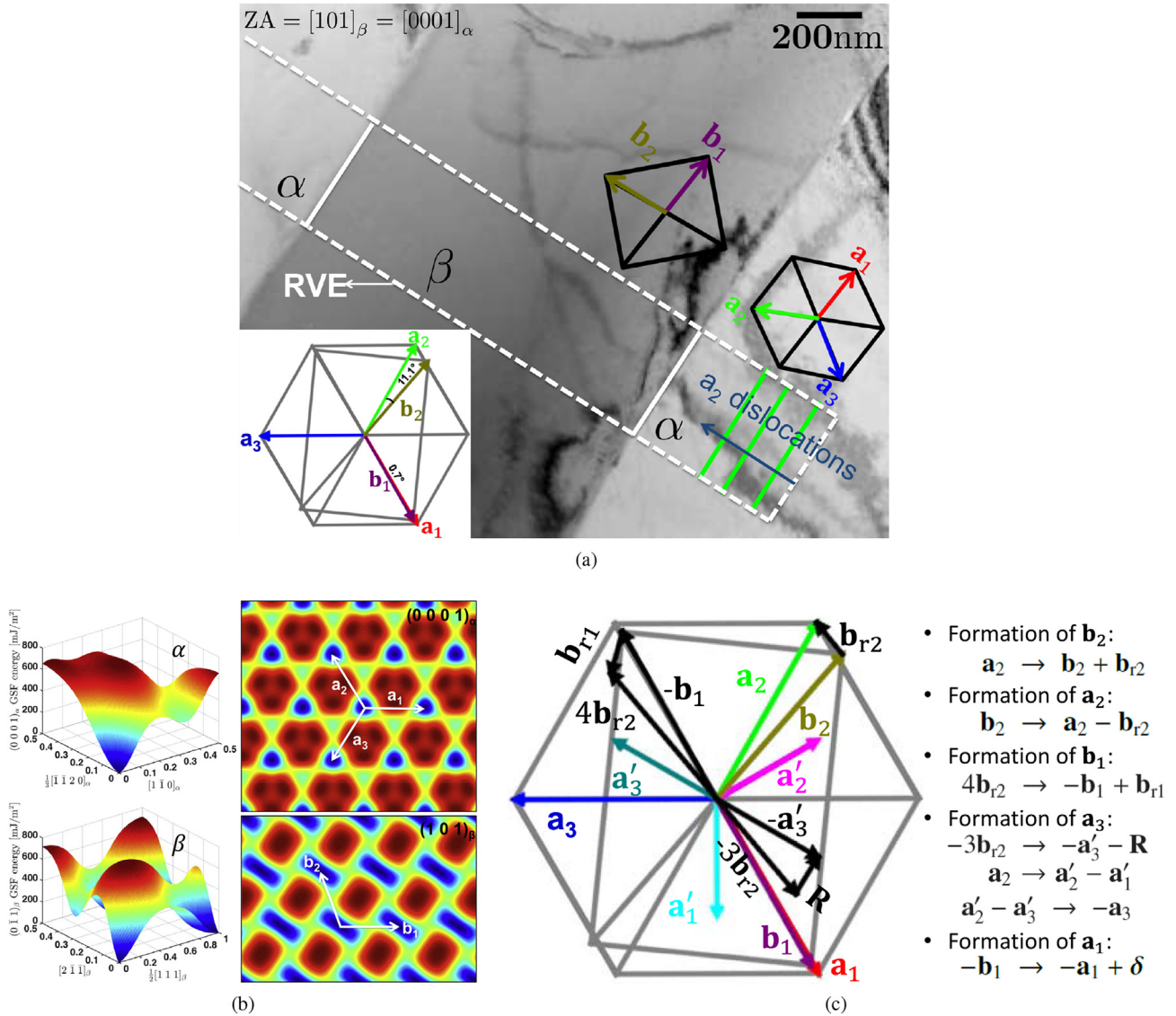
(a)

(b)

- Formation of $\mathbf{b}_2$:
  $$\mathbf{a}_2 \rightarrow \mathbf{b}_2 + \mathbf{b}_{r2}$$
- Formation of $\mathbf{a}_2$:
  $$\mathbf{b}_2 \rightarrow \mathbf{a}_2 - \mathbf{b}_{r2}$$
- Formation of $\mathbf{b}_1$:
  $$4\mathbf{b}_{r2} \rightarrow -\mathbf{b}_1 + \mathbf{b}_{r1}$$
- Formation of $\mathbf{a}_3$:
  $$-3\mathbf{b}_{r2} \rightarrow -\mathbf{a}_3' - \mathbf{R}$$
  $$\mathbf{a}_2 \rightarrow \mathbf{a}_2' - \mathbf{a}_1'$$
  $$\mathbf{a}_2' - \mathbf{a}_3' \rightarrow -\mathbf{a}_3$$
- Formation of $\mathbf{a}_1$:
  $$-\mathbf{b}_1 \rightarrow -\mathbf{a}_1 + \delta$$

(c)

Fig. 1. (a) The near-Burgers OR revealed by a bright-field TEM image along $(1\,0\,1)_\beta \parallel (0\,0\,0\,1)_\alpha$ zone axis in Ti6242 [3], together with a schematic illustration of the OR (inset). Note that the $0.7°$ angle between $\mathbf{a}_1$ and $\mathbf{b}_1$ separates this OR from the ideal Burger OR defined in Eq. (10). The dashed rectangle represents (part of) the simulation RVE, where a flat and sharp α/β interface is assumed and a flux of incoming $\mathbf{a}_2$-type straight dislocations are illustrated. (b) GSF energy surfaces of $\{0\,0\,0\,1\}_\alpha$ and $\{0\,\overline{1}\,1\}_\beta$, together with their matching to the near-Burgers OR on the common slip plane $(1\,0\,1)_\beta \parallel (0\,0\,0\,1)_\alpha$. (c) Maps of dislocation reactions involved in our slip transmission simulation, together with some key reactions being listed as well. Here $\mathbf{a}_1 = a_\alpha[2\overline{1}\overline{1}0]_\alpha/3$, $\mathbf{a}_2 = a_\alpha[\overline{1}2\overline{1}0]_\alpha/3$, and $\mathbf{a}_3 = a_\alpha[\overline{1}\overline{1}20]_\alpha/3$ are full dislocations on the basal planes of α and $\mathbf{a}_1' = a_\alpha[1\overline{1}00]_\alpha/3$, $\mathbf{a}_2' = a_\alpha[01\overline{1}0]_\alpha/3$, and $\mathbf{a}_3' = a_\alpha[\overline{1}010]_\alpha/3$ are the Shockley partials; $\mathbf{b}_1 = a_\beta[1\overline{1}1]_\beta/2$ and $\mathbf{b}_2 = a_\beta[\overline{1}11]_\beta/2$ are the full dislocations on the $(1\,0\,1)$ plane of β; the rest dislocations are residual dislocations at the interface due to reactions that will be discussed in Section 4.

dislocations. For the $\mathbf{a}_1$ dislocations (see the definition in Fig. 1a), owing to the nearly perfect alignment between $\mathbf{a}_1$ and $\mathbf{b}_1$ as well as the close match between the magnitudes of the Burgers vectors in α and β, i.e., $b_\beta = 0.9472b_\alpha$, slip transmission is expected to occur easily; the lack of a $\frac{a_\beta}{2}\langle 1\,1\,1\rangle_\beta$ slip system that is closely aligned with $\mathbf{a}_3$ suggests a difficulty of slip transmission. These intuitive expectations based on the near-Burger OR have been confirmed by the experiments [3]. In our current work, we will focus particularly on the transmission of $\mathbf{a}_2$ dislocations, which according to the OR will match $\mathbf{b}_2$ but with a much larger deviation angle as compared to that between $\mathbf{a}_1$ and $\mathbf{b}_1$. In addition, since the $\mathbf{a}_2$ dislocations at the α/β interface are found to exhibit narrow loop-like configurations elongated along the screw orientation [3], it is sufficient to approximate the line direction of $\mathbf{a}_2$-type dislocations as parallel to the interface, which leads to an effectively pseudo-2D simulations as indicated in Fig. 1a. However, the elastic energy calculation is still

rigorously done in 3D as described in Section 2.1.

Finally, unlike slip transmission in conventional polycrystals where the transmitted dislocation will most likely interact with an obstacle inside the (large enough) grain before it arrives at the next interface (grain boundary), the mean free path of dislocations in a single colony of α/β Ti-alloys can be comparable to the distances between adjacent α/β interfaces. This means that the newly transmitted dislocations will continuously interact at the next interface with the residual dislocations deposited by previously transmitted dislocations. As a result, we will use an " $\alpha \mid \beta \mid \alpha \mid \beta \mid \alpha$ " layered lamellar structure instead of a simple " $\alpha \mid \beta \mid \alpha$ " configuration. The significance of using such RVE will be borne out later.

3. Results

A slip transmission simulation is carried out using an

" $\alpha \,|\, \beta \,|\, \alpha \,|\, \beta \,|\, \alpha$ " layered lamellar structure (Fig. 2a), where the width is $486.9b_\alpha = 143.7$nm for the β lath and $1947.6b_\alpha = 574.7$nm for the α lath. In the simulation, the grid spacing is chosen to be 0.0702nm and the time step is 0.1 in a reduced unit. Periodic boundary condition (PBC) is used for the FFT-based implementation, but the "image effect" is largely removed by ensuring a large enough RVE (here we use 20480 grid points for our pseudo-2D simulations) with the order parameter at one end of the computational cell being frozen. (This technique is used previously in predicting dislocation core structures [27] and is proven to be accurate by comparing with the atomistic simulations.) The dimensions of our RVE are in the same order of magnitude as the microstructural characteristics revealed experimentally in Ref. [3]. A flux of incoming discrete $\mathbf{a}_2$ dislocations are continuously introduced into the RVE from one bound at a constant rate of $10^{-3}/t^*$ (t^* is the reduced time) and the total simulation time is $t^* = 2.4 \times 10^4$. (In other words, 24 incoming $\mathbf{a}_2$ dislocations are evenly introduced during the simulation.) The applied external shear stress is along the $\mathbf{a}_2$ direction and has a value of 420 MPa, which is slightly higher than the experimentally measured 405 MPa for the critical resolved shear stress in Ref. [3]. Note that the incoming dislocations are introduced at locations far way from the interface. This will eliminate the effect of different rates at which new dislocations are introduced, which can only modify the local stress state and interdislocation spacing in the initial stage. As incoming dislocations arrive at the interface, the configuration and stress state should still be controlled by the externally applied stress.

Figure 2a summarizes the simulation results schematically, where the overall dislocation types presented in each phase regions are illustrated and the length of the arrows represent schematically the amount of the corresponding dislocation types. (Note that residual dislocations, which usually do not belong to any type of lattice dislocations, are not shown in Fig. 2a.) In the following, we present the detailed dislocation transfer events occurring at the four interfaces as denoted by **I-1**, **I-2**, **I-3**, and **I-4** in Fig. 2a and leave the analysis of the underlying mechanisms to the next section.

3.1. Slip transmission across interface I-1: $\alpha \rightarrow \beta$

At **I-1**, a flux of $\mathbf{a}_2$ dislocations in α are constantly traveling toward β. In Fig. 3 (and similar figures in the following), misfit energy due to lattice disregistry are plotted at instants of interest, where peaks in the energy profile correspond to the dislocation cores. Figures 3a and 3b show the first slip transmission event at **I-1**, where incoming $\mathbf{a}_2$ in α (Fig. 3a) is successfully transmitted and an outgoing $\mathbf{b}_2$ is formed in β (Fig. 3b). A residual dislocation is then deposited at the interface, which is shown in detail in the inset of Fig. 3b. It is seen that only a much smaller misfit energy (compared to that due to a lattice dislocation) is associated with the residual dislocation, consistent with the fact that $\mathbf{a}_2$ and $\mathbf{b}_2$ do not differ much from each other as shown in the near-Burgers OR (Fig. 1a). In addition, the residual dislocation is asymmetrically spread over a region of $\sim 2b$ at the interface and composed of "components" (unit vectors) of various Burgers vectors of both α and β (colored differently), owing to the different GSF energy surfaces of the two phases. In fact, the center of the residual dislocation (where a peak of misfit energy is present) is shown to be inside β rather than at the interface.

Note that in Fig. 3, there are some non-zero background misfit energy present in both α and β, which are due to the elastic distortion caused by the applied shear stress. It has been confirmed in our simulations that a lower applied stress level results in a smaller background energy. The reason why this background energy is more significant in β than in α is due to the fact that the applied shear stress is perfectly aligned along $\mathbf{a}_2$. It will be seen in the following (with more detailed explanation) that this applied shear stress will significantly change the core structure of $\mathbf{b}_2$ but not that of $\mathbf{a}_2$. Such influence of elasticity on the equilibrium dislocation configuration in MPF is physical because according to the Peierls model the finite dislocation core results from exactly the competition between the fault energy and elastic energy, and has been shown by the previous study [27]. It also needs to be pointed out that the full $\mathbf{a}$-type dislocations will dissociate into two Shockley partials following (Fig. 1c)
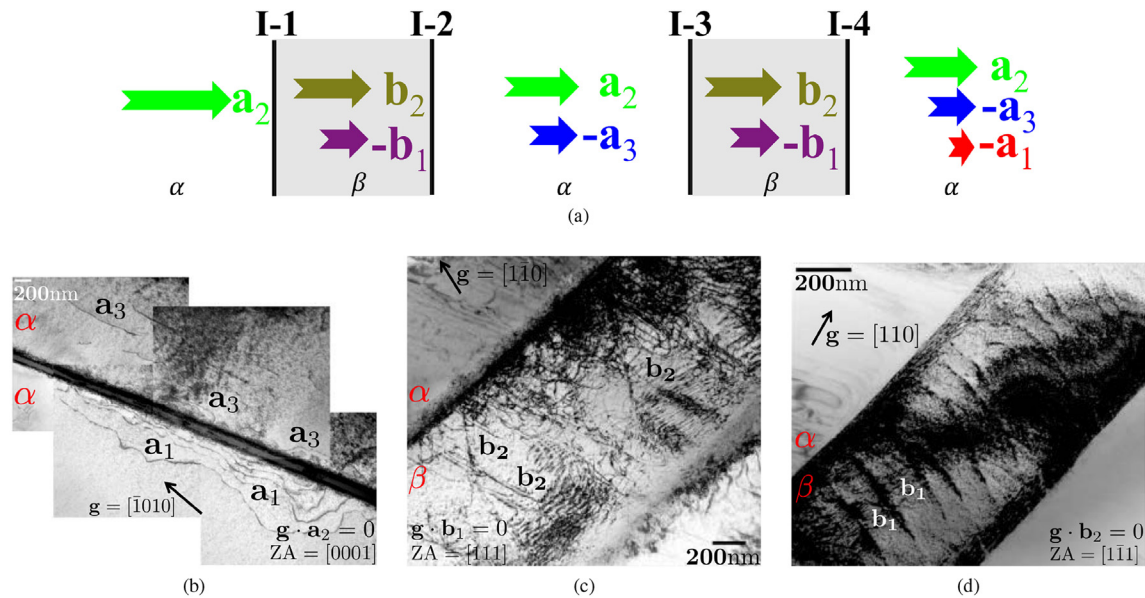

Fig. 2. (a) Summary of the dislocation types presented in each regions during MPF modeling of slip transmission, where the length of arrows illustrate schematically the amount of the corresponding dislocation type. (b) TEM image showing $\mathbf{a}_1$ and $\mathbf{a}_3$ dislocations located on two sides of the β lath (the thin dark lath). (c) TEM image showing pileups of edge character $\mathbf{b}_2$ dislocations at the exit α/β interface, together with a lower content of screw character $\mathbf{b}_2$ dislocations. (d) TEM image showing the presence of $\mathbf{b}_1$ dislocations with a much lower content than $\mathbf{b}_2$ in (c). All TEM images are adopted from Ref. [42] with appropriate annotation being added.
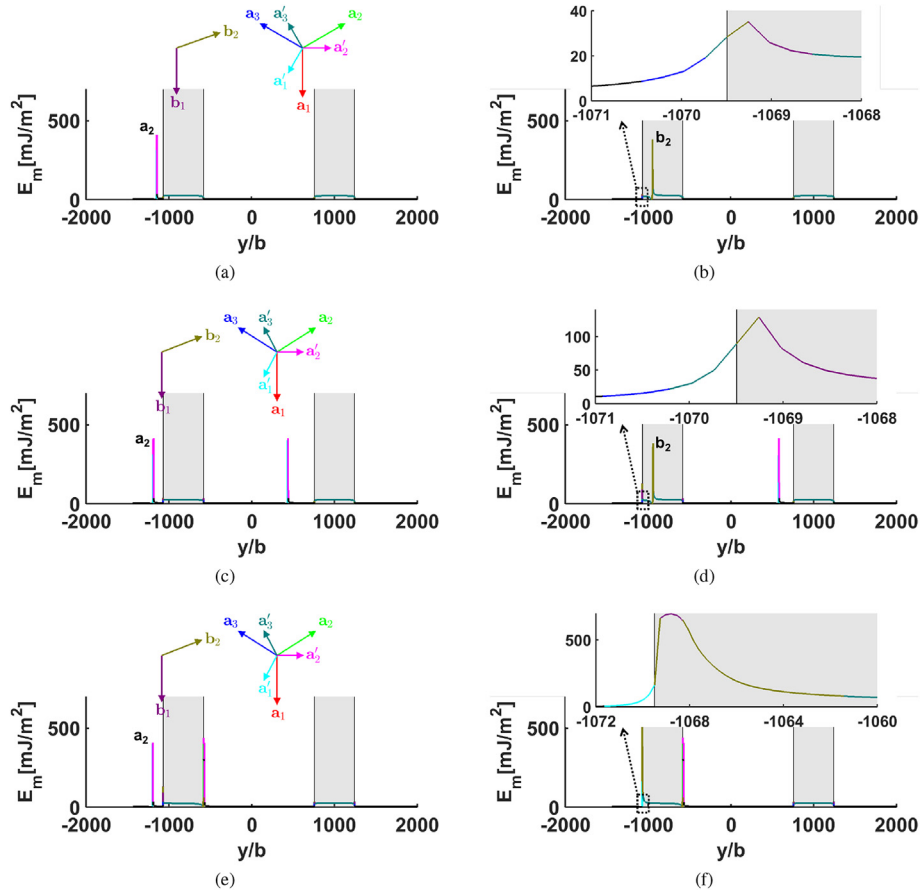
Fig. 3. Misfit energy due to lattice disregistry (a) before and (b) after the first slip transmission event at **I-1**, where peaks correspond to the dislocation cores. A residual dislocation after the transmission is shown in detail in the inset of (b). Note that the misfit energy plot is colored corresponding to the dislocation type; if the misfit energy is below a threshold, it is regarded as zero Burgers vector density and plotted in black. (c)–(d) Transmission of the second incoming **a**₂ across **I-1**, resulting in an outgoing **b**₂ with a residual dislocation shown in the inset of (d). (e)–(f) The third incoming **a**₂ cannot transmit across and is halted at the interface, with the inset of (f) showing the detailed configuration of the dislocation halted at the interface.

$$\frac{a_\alpha}{3}\left[2\,\overline{1}\,\overline{1}\,0\right]_\alpha \rightarrow \frac{a_\alpha}{3}\left[1\,\overline{1}\,0\,0\right]_\alpha - \frac{a_\alpha}{3}\left[\overline{1}\,0\,1\,0\right]_\alpha, \tag{11}$$

$$\frac{a_\alpha}{3}\left[\overline{1}\,2\,\overline{1}\,0\right]_\alpha \rightarrow \frac{a_\alpha}{3}\left[0\,1\,\overline{1}\,0\right]_\alpha - \frac{a_\alpha}{3}\left[1\,\overline{1}\,0\,0\right]_\alpha,$$

$$\frac{a_\alpha}{3}\left[\overline{1}\,\overline{1}\,2\,0\right]_\alpha \rightarrow \frac{a_\alpha}{3}\left[\overline{1}\,0\,1\,0\right]_\alpha - \frac{a_\alpha}{3}\left[0\,1\,\overline{1}\,0\right]_\alpha.$$

However, due to the plotting at a much larger length scale, the dissociated core structure is not readily seen in Fig. 3. We will present these detailed dislocation cores in Section 4 when analyzing the underlying reactions, but simply denote as the full dislocation on the dislocation dynamics plotting (e.g., **a**₂ in Fig. 3) in this section.

As the second incoming **a**₂ arrives at **I-1**, the simulation predicts that slip transmission can still occur in spite of the presence of a residual dislocation at the interface, as shown in Figs. 3c and 3d. This second slip transmission event will leave another residual dislocation, which, combined with the previous one, is shown in detail in the inset of Fig. 3d. This net residual dislocation is much larger in magnitude, indicated by a much higher associated misfit energy, as compared to that left by the first slip transmission event (Fig. 3b). Because of this "longer" residual dislocation, the third incoming **a**₂ (Fig. 3e) turns out to be unable to transmit across **I-1**

and is halted at the interface, as shown in Fig. 3f. The widespread (∼ 10b) internal structure of the net dislocation at the interface (the inset of Fig. 3f) suggests that the total (required) displacement (∼ b) is accommodated by significant elastic distortion, which is primarily located in β. This is in sharp contrast to the core structure of the lattice dislocation in both phases.

Upon the fourth incoming **a**₂ traveling towards the interface (Fig. 4a), the local stress at **I-1** is increased because of the elastic interaction with the incoming dislocation. This leads to the release of the previously halted dislocation due to the third incoming **a**₂ (Fig. 3f), which occurs even before the fourth incoming **a**₂ arrives at the interface, as shown in Fig. 4b. After this slip transmission, the residual dislocation at **I-1** (the inset of Fig. 4b) is significantly "shortened" as compared to the previously halted dislocation (Fig. 3f). Consequently, the fourth incoming **a**₂ continues to approach the interface (Fig. 4c) and eventually transmit across the interface. However, in contrast to previous cases, this slip transmission event results in two outgoing lattice dislocations in β, i.e., **b**₂ and −**b**₁ as shown in Fig. 4d. The large separation between **b**₂ and −**b**₁ is due to the fact that the resolved shear stress of **b**₂ is significantly larger than that of −**b**₁, resulting in obviously different velocities. As a result, our simulation shows that the constant flux of **a**₂ can initially transmit **I-1** easily, then halt for a while, and finally transmit again, with overall both **b**₂ and −**b**₁ being formed as the outgoing dislocations.
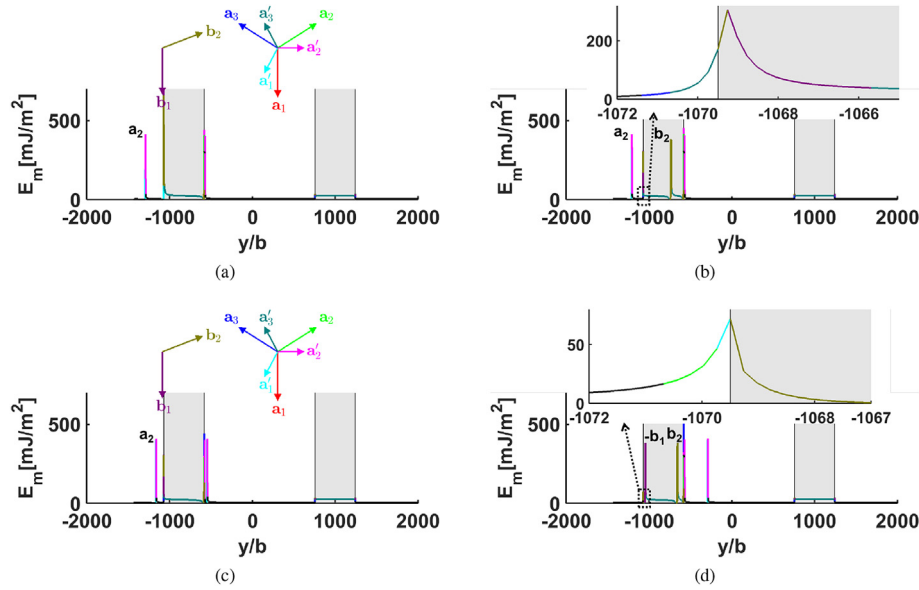
Fig. 4. Slip transmission upon the approaching of (a) the fourth incoming $\mathbf{a}_2$ towards **I-1**. The increased elastic interaction, even before the arrival of $\mathbf{a}_2$, promotes (b) the release of the previously halted dislocation (the third incoming $\mathbf{a}_2$), forming an outgoing $\mathbf{b}_2$, with a significantly "shortened" residual dislocation shown in the inset of (b). The fourth incoming $\mathbf{a}_2$ (c) continues to approach the interface and (d) successfully transmit across the interface, resulting two outgoing lattice dislocations: $\mathbf{b}_2$ and $-\mathbf{b}_1$.

3.2. Slip transmission across interface I-2: $\beta \rightarrow \alpha$

The transmitted $\mathbf{b}_2$ and $-\mathbf{b}_1$ across **I-1** will continuously travel towards **I-2** due to the applied shear stress. Figure 5a shows the first incoming $\mathbf{b}_2$, which, under the applied stress, transmits across **I-2** successfully and becomes $\mathbf{a}_2$ as shown in Fig. 5b. A residual dislocation is then deposited at the interface, as shown in the inset of Fig. 5b, which exhibits a core region of $\sim 2b$, similar to that of the first transmission event at **I-1** as shown in Fig. 3b. However, the center of this residual dislocation is right at the interface, which differs from that shown in Fig. 3b.

As the second incoming $\mathbf{b}_2$ arrives at **I-2**, however, slip transmission cannot continue and the lattice dislocation is halted at the interface, as shown in Figs. 5c and 5d. The resulting halted dislocation at the interface exhibits a widespread internal structure of $\sim 15b$ as shown in Fig. 5d, suggesting a considerable elastic contribution to this core structure. This feature is similar to the halted dislocation at **I-1** as shown in Fig. 4b. However, the latter exhibits only a single-peak core, while a double-peak core is seen in Fig. 5d. When the third incoming $\mathbf{b}_2$ arrives at **I-2** with a previously halted $\mathbf{b}_2$ (Fig. 5e), slip transmission occurs by releasing an outgoing $\mathbf{a}_2$ but again halting the new incoming $\mathbf{b}_2$, as shown in Fig. 5f. It can be seen that there is a slight difference in terms of the core structure of the new halted dislocation at **I-2** as compared to that in Fig. 5d, which is due to the fact that release of a $\mathbf{a}_2$ will add a small residual dislocation to the interface.

The fourth incoming $\mathbf{b}_2$, shown in Fig. 6a, is found to result in the release of two outgoing lattice dislocations, $\mathbf{a}_2$ and $-\mathbf{a}_3$, as shown in Fig. 6b. This is because there is already a previous $\mathbf{b}_2$ halted at the interface before the fourth incoming $\mathbf{b}_2$ undergoes slip transmission. The formation of $-\mathbf{a}_3$ is non-trivial and will be analyzed in Discussion section. The next incoming dislocation is of type $-\mathbf{b}_1$ as shown in Fig. 6c, which is halted at the interface as shown in Fig. 6d. The detailed core structure of this halted dislocation (the inset of Fig. 6d) shows that the incoming $-\mathbf{b}_1$ is still entirely located in β but only $\sim 4b$ away from the interface; the net residual dislocation left by the previous slip transmissions is, on the other hand, entirely located in α. This suggests that there is a strong elastic repulsion between $-\mathbf{b}_1$ and the interface residual dislocation, which prevents

the transmission of the former. Nevertheless, the slip transmission of the sixth incoming dislocation of type $\mathbf{b}_2$ (Fig. 6e) is not affected by the halted $-\mathbf{b}_1$ and results in another outgoing $\mathbf{a}_2$ as shown in Fig. 6f. Overall, other than $\mathbf{a}_2$ and $-\mathbf{a}_3$, we do not see any new types of lattice dislocations being transmitted across **I-2** upon further simulation.

3.3. Slip transmission across interface I-3: $\alpha \rightarrow \beta$

While **I-3** is geometrically identical to **I-1**, the slip transmission is in fact not identical to these two interfaces, owing to the fact that the types of incoming dislocations are different, as indicated in Fig. 2a. There is an additional $-\mathbf{a}_3$ type incoming dislocations for **I-3**. Fig. 7 shows the slip transmission of a $-\mathbf{a}_3$ type incoming dislocation across **I-3**, which results in an outgoing $\mathbf{b}_2$ dislocation. While the presence of incoming $-\mathbf{a}_3$ do not change the overall types of transmitted dislocations across **I-3** as compared to those across **I-1** (Fig. 2a), the sequence of the transmitted dislocations are clearly changed, which will eventually alter the dislocation transfer in the subsequent **I-4** as will be discussed in the next section. Note that the residual dislocation (the inset of Fig. 7b) after the transmission of $-\mathbf{a}_3$ exhibits a similar core structure as that shown in Fig. 4d. However, the latter is obtained after an outgoing $-\mathbf{b}_1$ is released from the interface, which is completely different from the case shown in Fig. 7.

3.4. Slip transmission across interface I-4: $\beta \rightarrow \alpha$

Given the same incoming dislocation types of $\mathbf{b}_2$ and $-\mathbf{b}_1$ as those of **I-2**, the slip transmission at **I-4** bears much similarity to that at **I-2** in terms of the outgoing dislocation types of $\mathbf{a}_2$ and $-\mathbf{a}_3$. However, a distinctive feature at **I-4** is the formation of the $-\mathbf{a}_1$ outgoing dislocation, as indicated in Fig. 2a. This difference is originated from the fact that the sequence of the incoming dislocation types are changed due to the different slip transmission behaviors of **I-1** and **I-3**, as discussed in the previous section. In particular, while the $-\mathbf{b}_1$ type dislocation appears as the fifth incoming dislocation at **I-2** (Fig. 6c), **I-4** has to transmit nine $\mathbf{b}_2$ dislocations before seeing an incoming $-\mathbf{b}_1$. Figure 8a shows this
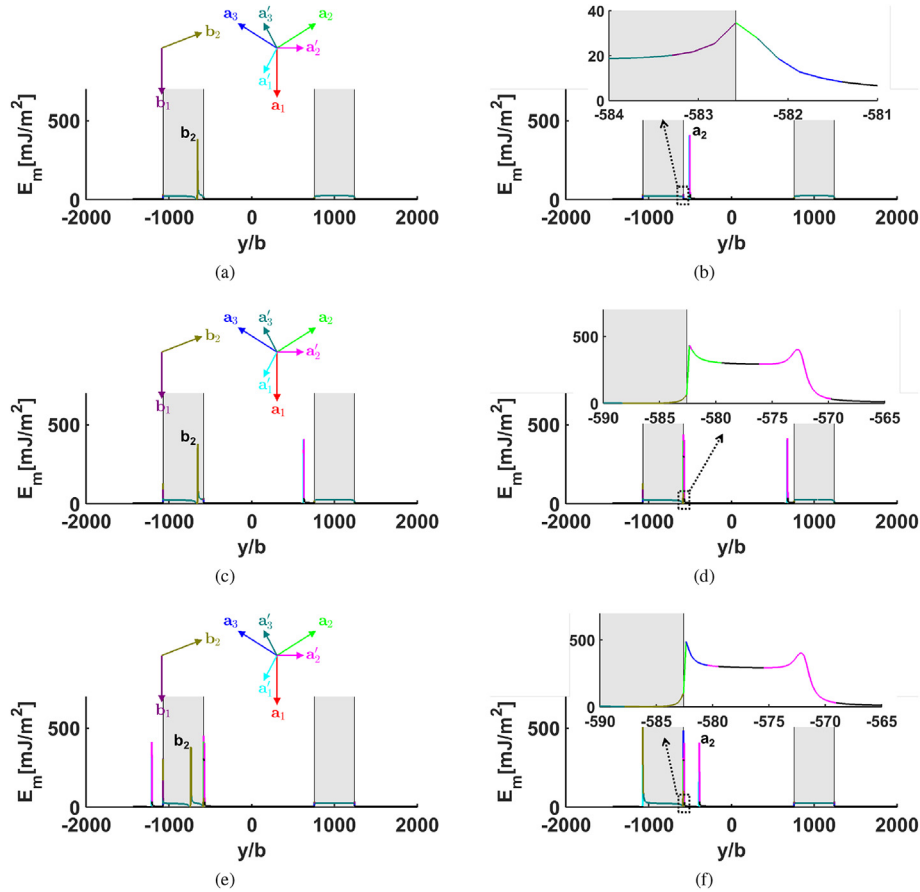
Fig. 5. (a)–(b) Transmission of the first incoming $\mathbf{b}_2$ across **I-2**, resulting in an outgoing $\mathbf{a}_2$ with a residual dislocation shown in the inset of (b). (c)–(d) The second incoming $\mathbf{b}_2$ of **I-2**, which cannot transmit across and is halted at the interface, with the inset of (d) showing the detailed dislocation structure at the interface. (e)–(f) As the third incoming $\mathbf{b}_2$ arrives, the previously halted $\mathbf{b}_2$ is released (to form an outgoing $\mathbf{a}_2$), at the cost of this third incoming $\mathbf{b}_2$ being halted at the interface as shown in the inset of (f).

first $-\mathbf{b}_1$ traveling towards **I-4** and followed by a $\mathbf{b}_2$. The two incoming dislocations result in an outgoing $\mathbf{a}_2$ and a halted dislocation at the interface as shown in Fig. 8b. This halted dislocation, primarily originated from the incoming $-\mathbf{b}_1$, is found to be unstable at the interface and starts to extend away from the interface as a new $\mathbf{b}_2$ is approaching **I-4**, as shown in Fig. 8c. The extended dislocation exhibits two peaks that are separated by $\sim 80b$ but continuously joint by a faulted region in between, as shown in the inset of Fig. 8c. When the approaching $\mathbf{b}_2$ finally arrives at **I-4** (which turns out to be halted), the above extended dislocation quickly splits into two localized dislocations, with one being a residual dislocation at the interface and the other being inside α, as shown in Fig. 8d. During this split, the non-local elastic strain energy "collapses" into local (inelastic) core energy of dislocations, which is essentially the same physical process as that involved in the nucleation of dislocations at the expense of previously stored elastic energy [43,44]. The newly formed dislocation inside α (Fig. 8d) is found unstable and immediately split further into a $\mathbf{a}_2$ and $-\mathbf{a}_1$, as shown in Fig. 8e. In addition, the newly formed $\mathbf{a}_2$ and $-\mathbf{a}_1$ are further separated as shown in Fig. 8f, owing to the different resolved shear stresses and characters. Overall, all three $\mathbf{a}$-type dislocations are observed during slip transmission across **I-4**.

4. Discussion

4.1. Dislocation reactions during slip transmission

The formation of $\mathbf{b}_2$ at both **I-1** and **I-2** involves the following

dislocation reaction at the interface

$$\mathbf{a}_2 \rightarrow \mathbf{b}_2 + \mathbf{b}_{r2}, \tag{12}$$

where a residual dislocation $\mathbf{b}_{r2}$ is deposited at the interface. This is shown quantitatively in the reaction map of Fig. 1c. It is found that $\mathbf{b}_{r2} = (a_\alpha/150)[\overline{20}\,7\,13\,0]$, leading to $|\mathbf{a}_2|^2 > |\mathbf{b}_2|^2 + |\mathbf{b}_{r2}|^2$. According to the Frank's rule [45], Eq. (12) is energetically favorable, whereas its complementary reaction

$$\mathbf{b}_2 \rightarrow \mathbf{a}_2 - \mathbf{b}_{r2}, \tag{13}$$

occurring at both **I-2** and **I-4**, should be energetically unfavorable. However, the Frank's rule assumes isotropic elasticity and is essentially a geometric criterion, and does not account for the effect of external stress, which is the macroscopic driving force for slip transmission. Our current MPF modeling confirms that when subjected to a shear stress of 420 MPa (along $\mathbf{a}_2$), close to the experimental value of 405 MPa [3], both reactions of Eqs. (12) and (13) are energetically favorable. These reactions can be understood more clearly from Fig. 9, where the core configurations of $\mathbf{a}_2$ and $\mathbf{b}_2$ are plotted on the GSF energy surface of β. For comparison, core configurations subjected to a much lower stress (194 MPa) are also shown in Fig. 9. It is seen that at both stress levels the core configurations of $\mathbf{a}_2$ remain nearly identical, which is due to the fact that the applied shear is completely aligned with $\mathbf{a}_2$ and virtually does not change the minimum energy path of $\mathbf{a}_2$. In contrast, the core configurations of $\mathbf{b}_2$ changes significantly in response to the
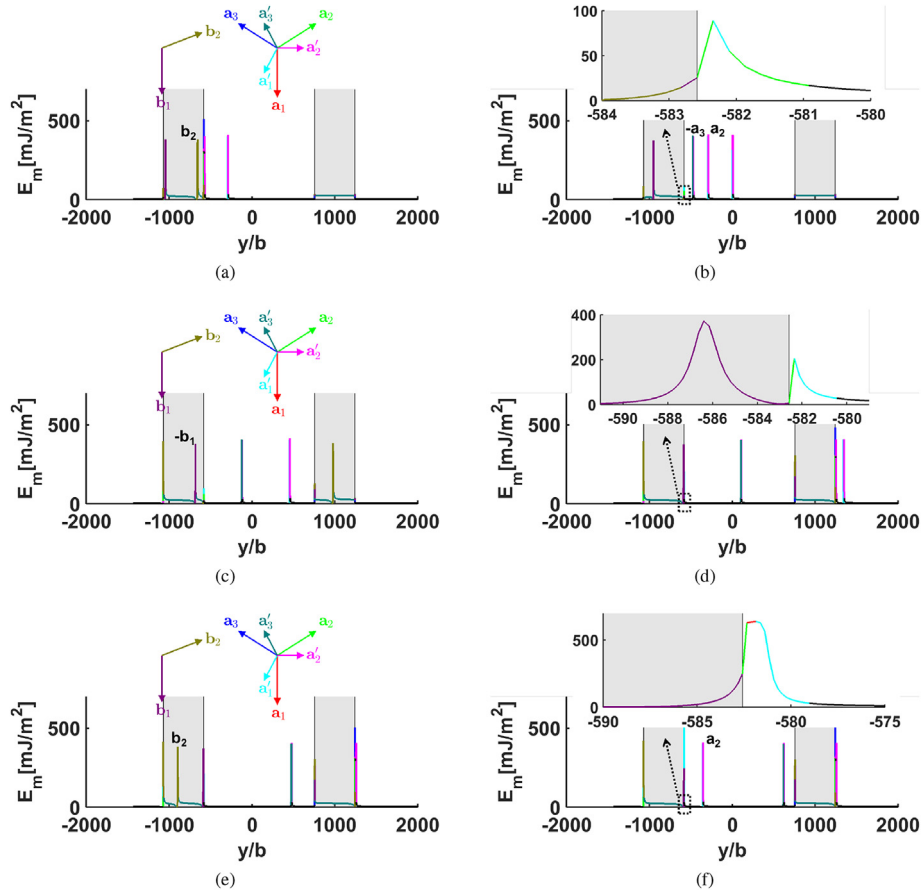
Fig. 6. Slip transmission of (a) the fourth incoming $\mathbf{b}_2$ of **I-2**, resulting in (b) two outgoing lattice dislocations: $\mathbf{a}_2$ and $-\mathbf{a}_3$. (c) The fifth incoming dislocation is of type (c) $-\mathbf{b}_1$, and is halted at the interface as shown in (d). (e) The transmission of the sixth incoming dislocation of type $\mathbf{b}_2$ is not affected by the halted $-\mathbf{b}_1$ and leads to an outgoing $\mathbf{a}_2$ as shown in (f).
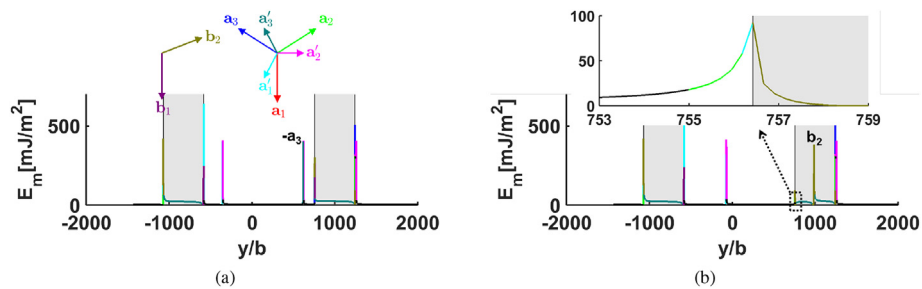

Fig. 7. Slip transmission of (a) an incoming $-\mathbf{a}_3$ of **I-3**, resulting in (b) an outgoing $\mathbf{b}_2$, with the residual dislocation shown in the inset of (b).

different stress levels due to an obvious mismatch between the shear stress direction and $\mathbf{b}_2$; a higher shear stress will bring $\mathbf{b}_2$ more towards the shear direction (i.e., more closer to $\mathbf{a}_2$ direction) instead of the MEP defined on the GSF energy surface. As a result, the reaction in Eq. (13) will occur more easily than predicted by the Frank's rule based purely on geometry.

The formation of $-\mathbf{b}_1$ at **I-1** and **I-3** is due to the consecutive storage of four $\mathbf{b}_{r2}$ (resulted from the reaction of Eq. (12)) following the reaction

$$4\mathbf{b}_{r2} \rightarrow -\mathbf{b}_1 + \mathbf{b}_{r1}. \tag{14}$$

This reaction may seem unfavorable based on the geometric consideration (Fig. 1c) according to the Frank's rule, but can actually occur when subject to sufficiently high stress as discussed

previously for the reaction of Eq. (13).

The formation of $-\mathbf{a}_3$ at **I-2** and **I-4** are found through three steps. The first step involves three consecutive reactions of Eq. (13), which leaves a net residual dislocation of $-3\mathbf{b}_{r2}$. It is then proposed that the following reaction occurs at the interface

$$-3\mathbf{b}_{r2} \rightarrow -\mathbf{a}'_3 - \mathbf{R}, \tag{15}$$

where a Shockley partial $-\mathbf{a}'_3$ is formed and $\mathbf{R} = (a_\alpha/150)[\overline{10}\,21\,\overline{11}\,0]$ is a residual dislocation. Based on the geometry as depicted in Fig. 1c, it is found that

$$|-\mathbf{a}'_3|^2 + |-\mathbf{R}|^2 - |-3\mathbf{b}_{r2}|^2 = 0.0067a_\alpha^2, \tag{16}$$

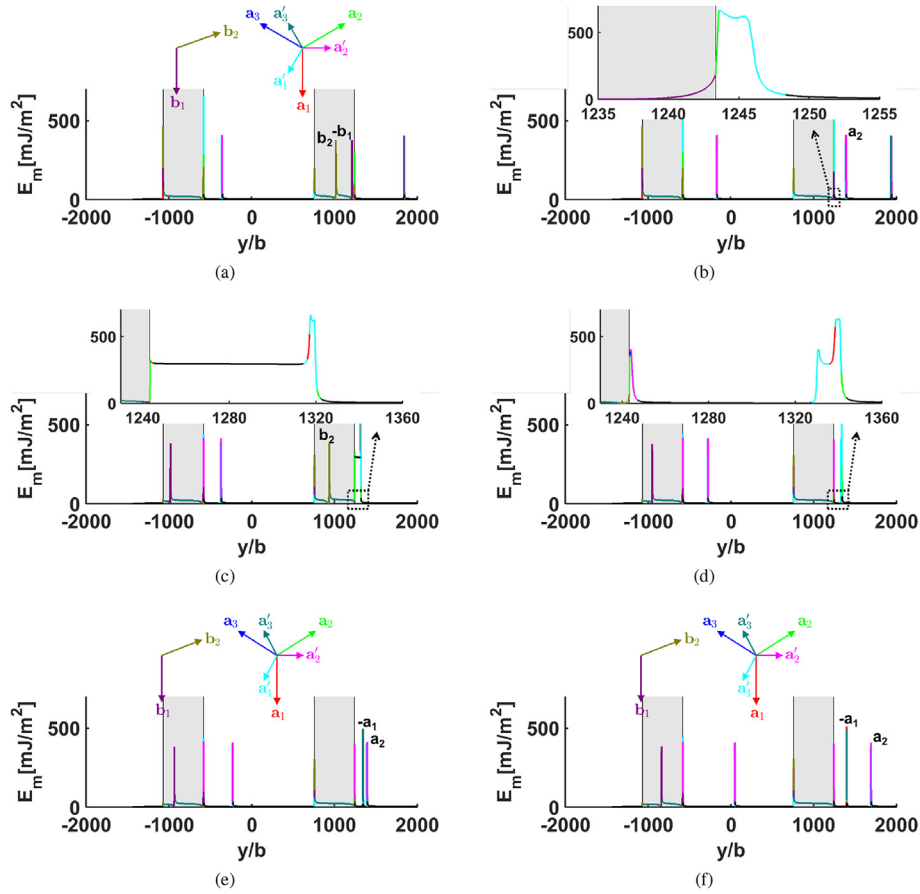which indicates that the reaction of Eq. (15) is almost energetically

Fig. 8. Slip transmission events at **I-4**. (a) Two consecutive incoming dislocations of type $-\mathbf{b}_1$ and $\mathbf{b}_2$, resulting in (b) an outgoing $\mathbf{a}_2$ and a halted dislocation (primarily due to the $-\mathbf{b}_1$) at the interface shown in the inset. (c) Influenced by a new incoming $\mathbf{b}_2$, the halted dislocation in (b) starts to adopt a highly extended internal structure, where two apparent peaks (of inelastic displacements), separated by $\sim 80b$, are continuously joint by a faulted region in between. (d) As the incoming $\mathbf{b}_2$ in (c) arrives at the interface (which is actually halted), the extended dislocation in (c) splits into two localized dislocations, with one being a residual dislocation at the interface and the other being inside α. (e) The latter then immediately dissociates into a $\mathbf{a}_2$ and $-\mathbf{a}_1$, which are further separated as shown in (f).
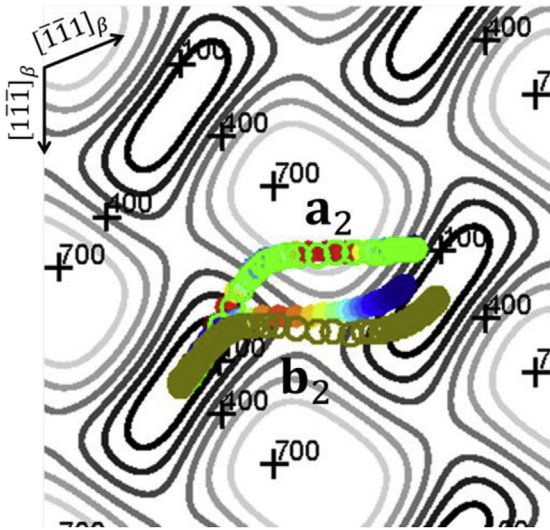

Fig. 9. Configurations of $\mathbf{a}_2$ and $\mathbf{b}_2$ core structures during the reaction of Eq. (12) plotted (filled circles) on the GSF energy surface (in units of mJ/m²) of β phase. The open circles show the corresponding core structures when the shear stress along $\mathbf{a}_2$ is lowered to 194 MPa as compared to 420 MPa used in obtaining data of filled circles.

neutral according to the Frank's rule. In addition, the resulting residual dislocation $\mathbf{R}$ is nearly parallel to $\mathbf{a}_2$, while the partial $-\mathbf{a}_3'$ is perpendicular to $\mathbf{a}_2$, which indicates that the applied shear stress along $\mathbf{a}_2$ should favor the proposed reaction of Eq. (15). In the third step, a new incoming $\mathbf{b}_2$ (towards **I-2** and **I-4**) will trigger another reaction of Eq. (13) and result in a new $\mathbf{a}_2$ that will dissociate into Shockley partials according to $\mathbf{a}_2 \rightarrow \mathbf{a}_2' - \mathbf{a}_1'$ as described in Eq. (11) and shown in Fig. 10a. The resulting $\mathbf{a}_2'$ will combine with $-\mathbf{a}_3'$ from Eq. (15) to give rise to a full dislocation $-\mathbf{a}_3$ following

$$\mathbf{a}_2' - \mathbf{a}_3' \rightarrow -\mathbf{a}_3, \tag{17}$$

which is simply the inverse of one of the reactions in Eq. (11). This mechanism is significantly different from the previously proposed one [2,3] (to be discussed and compared in Section 4.3) that did not consider Shockley partials.

The formation of $-\mathbf{a}_1$ at **I-4** (Fig. 8) is found to be represented by the following reaction

$$-\mathbf{b}_1 \rightarrow -\mathbf{a}_1 + \delta \tag{18}$$

where we use δ to denote an (small) accumulated residual dislocation at **I-4** (which is formed after eleven slip transmission events and thus difficult to identify in Fig. 1c). Eq. (18) is easy to understand and likely what to be expected according to the near-Burgers OR (Fig. 1a). However, an interesting prediction from our simulation is that no $-\mathbf{a}_1$ is formed at **I-2**, even though there are $-\mathbf{b}_1$ available
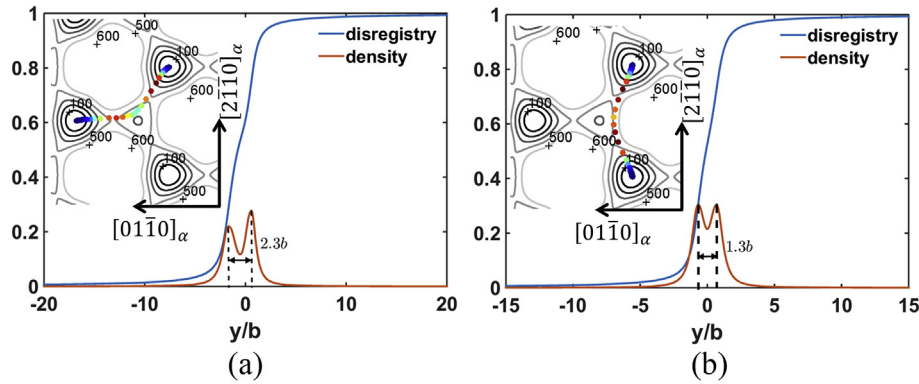
Fig. 10. The core structure of a straight (a) $\mathbf{a}_2$-type and (b) $\mathbf{a}_1$-type dislocation with the sense vector parallel to the α/β interface as illustrated in Fig. 1a. The insets show the corresponding configurations on the GSF energy surface (in units of mJ/m^2).

as the incoming dislocation. We have mentioned previously that this is due to the different sequences of the incoming $\mathbf{b}_2$ and $-\mathbf{b}_1$ of **I-2** and **I-4**. While at both interfaces, the incoming $-\mathbf{b}_1$ are halted as shown in Figs. 6f and 8b, the net residual dislocations left by previous transmissions are significantly different. During the subsequent slip transmission event with the same $\mathbf{b}_2-$type incoming dislocation, slip is successfully transmitted at **I-2** and leaves a residual $-\mathbf{b}_{r2}$ that partially neutralizes the halted $-\mathbf{b}_1$; in contrast, the incoming $\mathbf{b}_2$ is halted at **I-4** (Fig. 8d), which pushes the previously halted $-\mathbf{b}_1$ away from the interface due to the elastic repulsion and hence prevents it from being neutralized.

4.2. Crossover between $\mathbf{a}_2$ and $\mathbf{a}_1$

The $-\mathbf{a}_1$ formed in Fig. 2a is pure screw type, different from the other two $\mathbf{a}$-type dislocations that are mixed type. It has been observed that compared with the mixed or edge character, screw character $\mathbf{a}$-type dislocation has a significantly lower mobility, which is usually attributed to a non-planar core structure of $\mathbf{a}$-type screw dislocations [46,47]. In our current simulations, even without considering the non-planar core of screw character $\mathbf{a}$-type dislocations, we have found that the pure screw $-\mathbf{a}_1$ moves significantly slower than $\mathbf{a}_2$ and $-\mathbf{a}_3$ of the mixed character despite that the resolved shear stress on $-\mathbf{a}_1$ and $-\mathbf{a}_3$ are the same. This suggests that the elastic property difference between the screw and edge characters of $\mathbf{a}$-type dislocations can already make a significant difference in terms of dislocation mobility.

Because of the significantly slower motion of $-\mathbf{a}_1$, the subsequent $\mathbf{a}_2$ transmitted across **I-4** can actually catch up and then surpass the $-\mathbf{a}_1$ spatially, as shown in the consecutive frames in Figs. 11a-d. Note that because of the elastic interaction between the two dislocations, the misfit energy at the cores can change as the distance between the dislocations varies during the crossover process. The "saddle-point" configuration of this crossover is also shown in Fig. 11c, which suggests a "super-dislocation" of $-3\mathbf{a}'_1$ type. These features are essentially originated from the underlying reaction mechanism, which is elucidated by plotting the dislocation core configurations on the GSF energy surface before, at the saddle-point, and after the crossover in Figs. 11e, 11f, and 11g, respectively. In particular, based on the saddle-point configuration (Fig. 11f) it can be considered that the reaction essentially involves the position switch among three Shockley partials, i.e., from " $\mathbf{a}'_3 \mid -\mathbf{a}'_1 \mid \mathbf{a}'_2$ " to " $\mathbf{a}'_2 \mid -\mathbf{a}'_1 \mid \mathbf{a}'_3$ ". This interesting observation is a consequence of the complex interplay between inelastic shear at the dislocation core regions and the elastic interaction resulted from dislocations and the applied shear stress. It suggests that in the basal slip of Ti and Ti-alloys, the hardening due to dislocation pile-up model may

depend sensitively on the dislocation characters as well as the applied stress level.

4.3. Comparison with experiments and previous mechanisms

Our simulation predictions of the presence of $\mathbf{b}_1$ and $\mathbf{b}_2$ in β, together with their relative amounts shown in Fig. 2a, are consistent with the experimental characterization as shown in Figs. 2d and 2c by Savage et al. [3,42], where the reactions of Eqs. (12) and (13) are also used to explain the formation of $\mathbf{b}_1$ and its subsequent transmission to α. However, the mechanism of $\mathbf{b}_1$ formation was not considered for the $\mathbf{a}_2$ basal slip scenario in Refs. [3,42]. Our current work presents the first mechanism of the formation of $\mathbf{b}_1$ dislocations during the slip transmission of α/β Ti-alloys oriented for $\mathbf{a}_2$ basal slip.

The presence of $\mathbf{a}_1$ and $\mathbf{a}_3$, located on both sides of one β lath (Fig. 2a), are also consistent with the experimental characterization as shown in Fig. 2b (adopted from Ref. [42]). However, the formation mechanisms of the $\mathbf{a}_1$ and $\mathbf{a}_3$ revealed by our current MPF simulations are different from those present in Ref. [3], which was originally proposed by Suri et al. [2] and did not consider the involvement of Shockley partials. It is suggested in Ref. [2] that before the formation of $\mathbf{a}_1$ and $\mathbf{a}_3$, six incoming $\mathbf{a}_2$ dislocations have to pass through the β lath, resulting in six reactions of Eq. (12) and Eq. (13) at, respectively, the entrance and exit sides of the β lath. This results in the storage of six residual dislocations of $\mathbf{b}_{r2}$ at the entrance and six $-\mathbf{b}_{r2}$ at the exit. It is then further assumed that the following reaction

$$6\mathbf{b}_{r2} \rightarrow -\mathbf{a}_1 + \delta' \tag{19}$$

occurs at the entrance, where δ' represents a residual dislocation, and its complementary reaction

$$-6\mathbf{b}_{r2} \rightarrow \mathbf{a}_1 - \delta' \tag{20}$$

occurs at the exit. The $\mathbf{a}_1$ formed at the exit will then react with a previously transmitted $\mathbf{a}_2$ to form $-\mathbf{a}_3$. However, our current simulation suggests that when four residual dislocations of $\mathbf{b}_{r2}$ are accumulated at the interface, a $\mathbf{b}_1$ dislocation will be readily formed via the reaction of Eq. (14). In contrast, the formation of $\mathbf{b}_1$ cannot be addressed in the previous mechanism. Similarly, the formation of $\mathbf{a}_3$ in our current simulation requires only four incoming $\mathbf{a}_2$ dislocations passing through the β lath rather than six proposed in the previous mechanism. Finally, according to the mechanism in Ref. [3], the $\mathbf{a}_1$-type dislocation (e.g., see Fig. 2a) should always be on the entrance side and the $\mathbf{a}_3$-type always on the exist side,
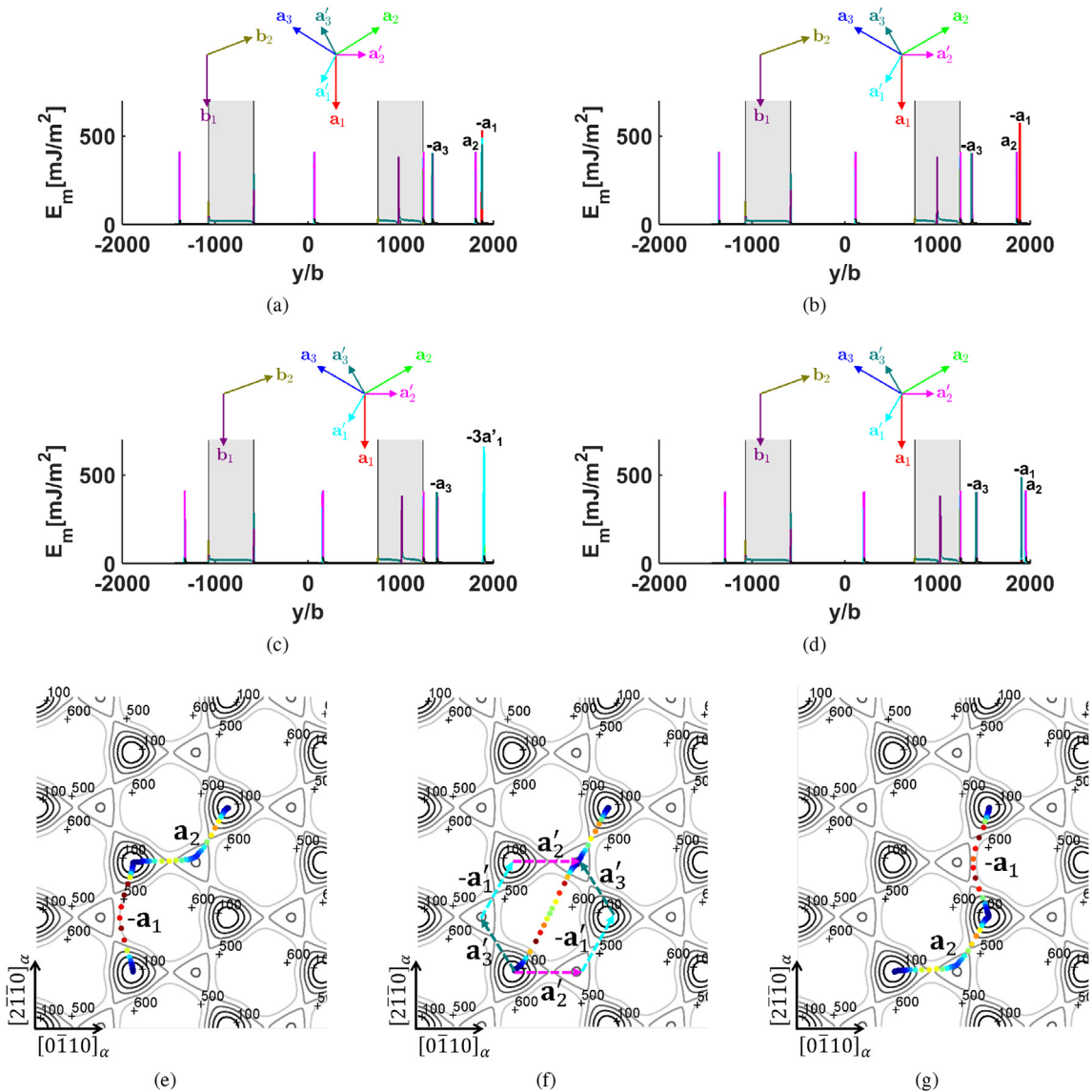
Fig. 11. Dislocation configurations of (a)–(d) four consecutive frames from the MPF simulation, showing the sequence of $\mathbf{a}_2$ crossing over $-\mathbf{a}_1$. The core configurations of dislocations involved are also plotted on the GSF energy surface (in units of mJ/m²) (e) before, (f) at the saddle-point of, and (g) after the cross-over.

which is opposite to our current MPF simulation. Because of the waviness of dislocation lines (and the possible relaxation in the thin sample foil), it is currently difficult to determine the entrance and exist sides based solely on the TEM image of Fig. 2b. In addition, because of the lack of pile-ups in the α phase for this orientation, determination of entrance/exit interface is not straightforward. Indeed, in situ experiments may be required to definitively make this determination. The current modeling results therefore motivate such additional experiments. It should also be pointed out that the mechanistic analysis in Ref. [3] is based on the dislocation configurations characterized in an RVE of "$\alpha | \beta | \alpha$", whereas a larger RVE of "$\alpha | \beta | \alpha | \beta | \alpha$" is used in the current simulation. It is obvious from the current results that a simulation using a simple "$\alpha | \beta | \alpha$" RVE cannot predict the formation of $\mathbf{a}_1$ at the exit interface (**I-2** in Fig. 2a). In addition, adding another "$\alpha | \beta | \alpha$" lamellar structure to the current "$\alpha | \beta | \alpha | \beta | \alpha$" RVE will not produce any new results because the $-\mathbf{a}_1$ and $-\mathbf{a}_3$ transmitted across **I-4** will reaction to form $\mathbf{a}_2$, leading to exactly the same incoming dislocation type for the newly added "$\alpha | \beta | \alpha$" lamellar

structure as compared to that for **I-1**.

4.4. Influence of stacking fault energy on the strength of α/β interface

Owing to the well alignment of slip systems in α and β, the α/β interfaces are usually considered to provide little hindrance to slip transmission and hence overall hardening. In contrast, the colony-colony boundary is a more effective hardening agent [48] and strengthening Ti-alloys is usually achieved via tailoring the texture at the colony size [49]. Since our current simulations suggest a critical role played by Shockley partials in assisting slip transmission across α/β interfaces, factors that control the dissociation of full dislocations into Shockley partials may thus influence the slip transmission process and hence the strength of α/β interfaces. We carry out a parametric study by systematically lowering the intrinsic stacking fault energy on the GSF energy surface of α, which will lead to a much larger separation between the dissociated Shockley partials in Eq. (11). (The GSF energy surface of β is kept

unchanged.) The modified GSF energy surface of α and its comparison with the original one are shown in Figs. 12a and 12b, respectively. The predicted core structures of **a**-type dislocations using the modified GSF energy surface are shown in Figs. 12c and 12d. Compared to the results in Fig. 10, it is obvious that due to the significantly lowered intrinsic stacking fault energy, the separation between the two Shockley partials is greatly increased.

The subsequent modeling of slip transmission, with exactly the same simulation setup in Section 3 except for using the modified GSF energy surface of α, exhibits some drastically different features and the overall transmitted dislocation types are summarized schematically in Fig. 12e. Owing to the low intrinsic stacking fault energy, decorrelated movements of two Shockley partials (originating from a full dislocation as in Eq. (11)) have been observed. Figure 13 is an example of a decorrelated Shockley partial $\mathbf{a}_2'$ that eventually arrives at **I-3**, whereas its pair $-\mathbf{a}_1'$ is halted at **I-2** during the process. In fact,
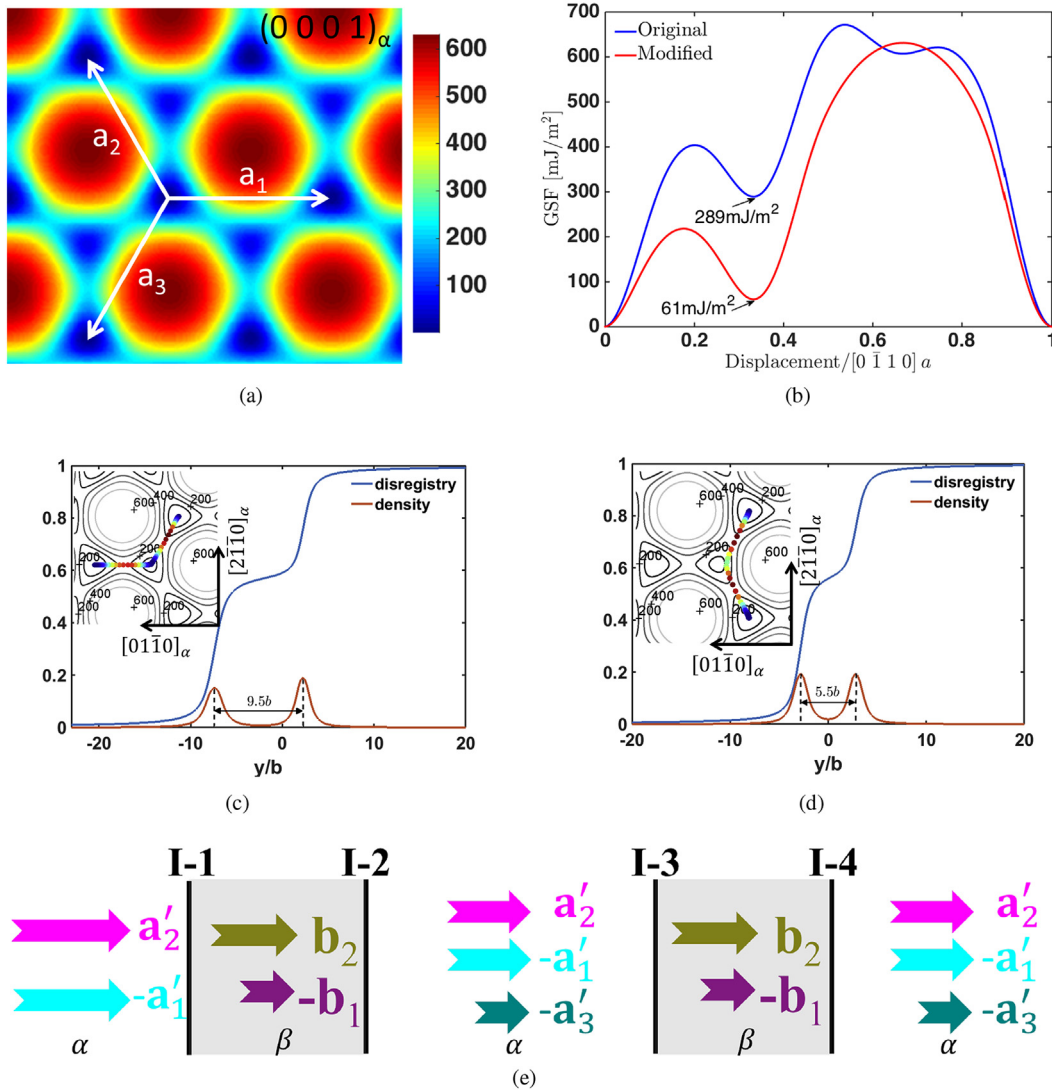

(a)

(b)

(c)

(d)

(e)

Fig. 12. (a) Modified GSF energy surface with a reduced intrinsic stacking fault energy (in units of mJ/m²). (b) Comparison between the original and modified GSF energy along $[0\,\bar{1}\,1\,0]$, where the intrinsic stacking fault energy values are indicated. The core structure of a straight (c) $\mathbf{a}_2$-type and (d) $\mathbf{a}_1$-type dislocation (compared to Fig. 10) using the modified GSF energy surface. (e) Summary of the dislocation types presented in each regions during MPF modeling of slip transmission using the modified GSF energy surface.
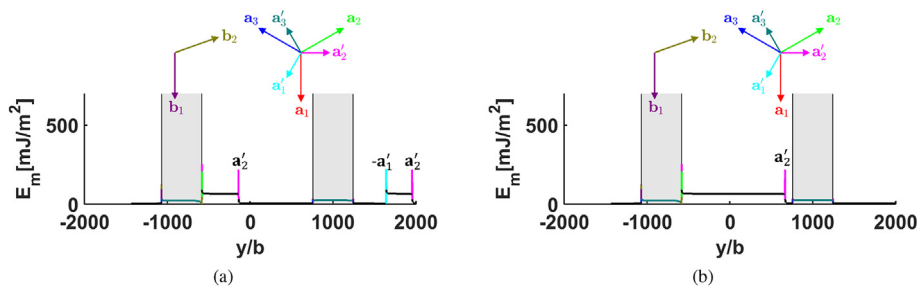

(a)

(b)

Fig. 13. Two consecutive frames showing the movement of a decorrelated Shockley partial $\mathbf{a}_2'$.

the tendency of such decorrelation is also manifested from the significantly increased core width of the dissociated $\mathbf{a}_2$ ($\rightarrow \mathbf{a}_2' - \mathbf{a}_1'$) shown in Fig. 13a as compared to the core width in Fig. 12c under no applied stress. In addition, it is observed that all three decorrelated Shockley partials (i.e., $\mathbf{a}_1'$, $\mathbf{a}_2'$, $\mathbf{a}_3'$) can be present at the same time in the α lath as shown in Fig. 14. This is significantly different from the previous simulation results in Section 3, where Shockley partials are always correlated in pairs following the dissociation reactions (Eq. (11)), which allows the identification of the full dislocation types. In fact, similar decorrelated movements of Shockley partials have been observed in nickel-base superalloys [50,51] and are attributed to the low stacking fault energy as well.

To obtain a quantitative comparison in terms of the interface strength, we first count the number of dislocations transmitted across I-4 during the simulation and the results are plotted in Fig. 15a. It is seen that the two simulations suggest similar results, with the lower intrinsic stacking fault leading to a slightly smaller number of dislocations transmitted; the resulting slip transmission rates, shown in Fig. 15b, further exhibit varying values for both simulations and a slightly slower transmission rate in the later stage ($t^* > 1.6 \times 10^4$) when using the modified GSF energy surface. Since the hardening is largely controlled by the stored residual dislocations, we plot in Fig. 15c the evolution of the stored crystalline energy normalized by the core energy of $\mathbf{a}_2$, which is a measure of the dislocation content stored in the system. The result indicates that the lowered stacking fault energy actually leads to larger contents of stored dislocations that are mainly halted at the interfaces. While a definite correlation between the overall strength and stacking fault energy requires obviously more comprehensive studies, this parametric study does imply that lowing the stacking fault energy can significantly change the slip transmission sequence and increase the stored dislocation contents at the interfaces, thus offering a new strengthening strategy at the single colony level for Ti-alloys.

This new strengthening strategy may also be rationalized based on our current simulation results. The narrow dislocation cores ($\sim b$) of basal dislocations ensure that the dissociated Shockley partials are spatially localized and thus ready to switch positions among each other when two $\mathbf{a}$-type dislocations meet to react. If the stacking fault energy is lowered (for example, through alloying as shown by experiments [52]), the separation of the dissociated Shockley partials will be increased and the *locality* required for the dislocation reactions in aid of slip transmission may not be satisfied any more. This should lead to greater hindrance to slip transmission and hence higher hardening rate offered by the α/β interface. This new strengthening strategy can also be investigated by a multiscale modeling that incorporates the current MPF method in a coarse-grained dislocation density based constitutive model, similar to the absorption-desorption-transmission kinetic equations presented in Ref. [53] for interfacial dislocation density evolution, which can then be used in the crystal plasticity framework to predict the macroscopic properties of Ti-alloys.

5. Conclusions

Slip transmission across α/β interfaces is of critical importance to understanding the strength of Ti-alloys, and has been studied in this paper using the microscopic phase-field modeling. Major findings are summarized as follows.

1. Shockley partials are found to play an important role in the underlying dislocation transfer across α/β interfaces, which offer viable dislocation reactions (that have not been considered before) to effectively reduce the total amount of residual dislocations deposited at the interface. The simulated dislocation configurations agree well with the existing experiments, in terms of both dislocation types and relative contents.

2. The spatial cross-over between $\mathbf{a}$-type dislocations (on basal planes) in α phase is also predicted by the microscopic phase-field modeling. The critical dislocation configurations during
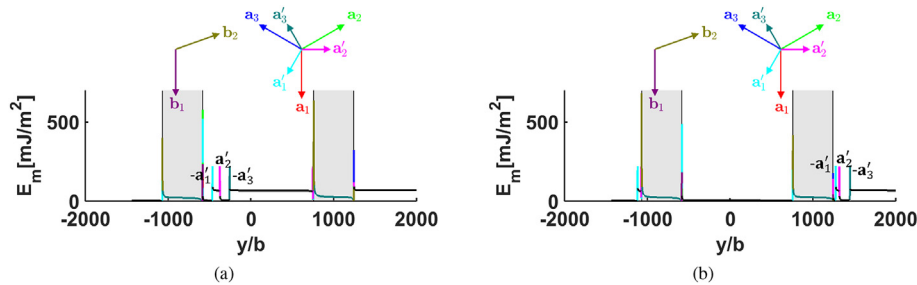

Fig. 14. All three types of Shockley partial are observed to transmit across (a) **I-2** and (b) **I-4**.
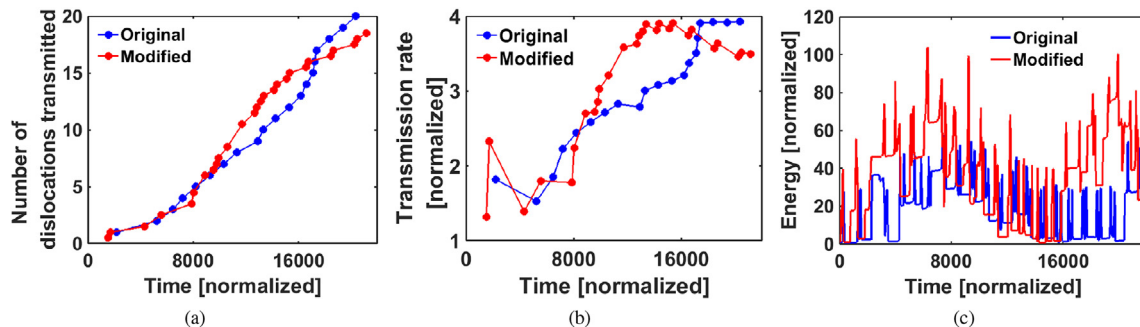

Fig. 15. Evolution of (a) the number of transmitted dislocations, (b) the normalized slip transmission rate, and (c) the stored crystalline (inelastic) energy normalized by the core energy of $\mathbf{a}_2$.

the cross-over are analyzed in details and the underlying reactions are revealed to be closely related to Shockley partials as well.

3. Based on a parametric study on the influence of stacking fault energy on slip transmission, a new strengthening strategy at the single α/β colony level is proposed, which suggests that lowering the stacking fault energy of the α phase (e.g., via alloying) may lead to greater hindrance of the α/β interface to dislocation transfer and hence a higher hardening rate.

4. The current study demonstrates the capability of microscopic phase-field modeling in revealing complex dislocation reactions and the underlying mechanisms by incorporating atomistic inputs, as well as its potential of being a complementary computational tool to experimental characterization on micro-analysis of plastic deformation.

Acknowledgements

References

[1] W. Miller, R. Chen, E. Starke, Microstructure, creep, and tensile deformation in Ti-6Al-2Nb-1Ta-0.8Mo, Metall. Trans. A 18 (1987) 1451–1468.
[2] S. Suri, G. Viswanathan, T. Neeraj, D.-H. Hou, M. Mills, Room temperature deformation and mechanisms of slip transmission in oriented single-colony crystals of an α/β titanium alloy, Acta Mater. 47 (1999) 1019–1034.
[3] M. Savage, J. Tatalovich, M. Mills, Anisotropy in the room-temperature deformation of $\alpha-\beta$ colonies in titanium alloys: role of the $\alpha-\beta$ interface, Phil. Mag. 84 (2004) 1127–1154.
[4] A.P. Sutton, Interfaces in crystalline materials, in: Monographs on the Physice and Chemistry of Materials, 1995, pp. 414–423.
[5] I. Beyerlein, M. Demkowicz, A. Misra, B. Uberuaga, Defect-interface interactions, Prog. Mater. Sci. 74 (2015) 125–210.
[6] I.J. Beyerlein, N.A. Mara, D. Bhattacharyya, D.J. Alexander, C.T. Necker, Texture evolution via combined slip and deformation twinning in rolled silver–copper cast eutectic nanocomposite, Int. J. Plast. 27 (2011) 121–146.
[7] S. Zheng, I. Beyerlein, J. Wang, J. Carpenter, W. Han, N. Mara, Deformation twinning mechanisms from bimetal interfaces as revealed by in situ straining in the tem, Acta Mater. 60 (2012) 5858–5866.
[8] A. Misra, J. Hirth, R. Hoagland, Length-scale-dependent deformation mechanisms in incoherent metallic multilayered composites, Acta Mater. 53 (2005) 4817–4824.
[9] J. Wang, A. Misra, An overview of interface-dominated deformation mechanisms in metallic multilayers, Curr. Opin. Solid State Mater. Sci. 15 (2011) 20–28.
[10] J. Livingston, B. Chalmers, Multiple slip in bicrystal deformation, Acta Metall. 5 (1957) 322–327.
[11] Z. Shen, R. Wagoner, W. Clark, Dislocation pile-up and grain boundary interactions in 304 stainless steel, Scripta Metall. 20 (1986) 921–926.
[12] E. Werner, W. Prantl, Slip transfer across grain and phase boundaries, Acta Metall. Mater. 38 (1990) 533–537.
[13] J. Luster, M. Morris, Compatibility of deformation in two-phase Ti-Al alloys: dependence on microstructure and orientation relationships, Metall. Mater. Trans. 26 (1995) 1745–1756.
[14] A. Misra, R. Gibala, Slip transfer and dislocation nucleation processes in multiphase ordered Ni-Fe-Al alloys, Metall. Mater. Trans. 30 (1999) 991–1001.
[15] E. Pacheco, T. Mura, Interaction between a screw dislocation and a bimetallic interface, J. Mech. Phys. Solids 17 (1969) 163–170.
[16] H. Chu, J. Wang, I. Beyerlein, E. Pan, Dislocation models of interfacial shearing induced by an approaching lattice glide dislocation, Int. J. Plast. 41 (2013) 1–13.
[17] J. Mayeur, I. Beyerlein, C. Bronkhorst, H. Mourad, B. Hansen, A crystal plasticity study of heterophase interface character stability of Cu/Nb bicrystals, Int. J. Plast. 48 (2013) 72–91.
[18] T. Bieler, P. Eisenlohr, C. Zhang, H. Phukan, M. Crimp, Grain boundaries and interfaces in slip transfer, Curr. Opin. Solid State Mater. Sci. 18 (2014) 212–226.
[19] J. Wang, R. Hoagland, J. Hirth, A. Misra, Atomistic modeling of the interaction of glide dislocations with weak interfaces, Acta Mater. 56 (2008) 5685–5693.
[20] M. Shehadeh, G. Lu, S. Banerjee, N. Kioussis, N. Ghoniem, Dislocation transmission across the Cu/Ni interface: a hybrid atomistic–continuum study, Phil. Mag. 87 (2007) 1513–1529.

[21] R.G. Hoagland, R.J. Kurtz, C.H. Henager, Slip resistance of interfaces and the strength of metallic multilayer composites, Scripta Mater. 50 (2004) 775–779.
[22] M.D. Sangid, T. Ezaz, H. Sehitoglu, I.M. Robertson, Energy of slip transmission and nucleation at grain boundaries, Acta Mater. 59 (2011) 283–296.
[23] Y. Zeng, A. Hunter, I.J. Beyerlein, M. Koslowski, A phase field dislocation dynamics model for a bicrystal interface system: an investigation into dislocation slip transmission across cube-on-cube interfaces, Int. J. Plast. 79 (2016) 293–313.
[24] Y.U. Wang, Y. Jin, A. Cuitino, A. Khachaturyan, Nanoscale phase field microelasticity theory of dislocations: model and 3D simulations, Acta Mater. 49 (2001) 1847–1857.
[25] C. Shen, Y. Wang, Phase field model of dislocation networks, Acta Mater. 51 (2003) 2595–2610.
[26] C. Shen, Y. Wang, Incorporation of γ-surface to phase field model of dislocations: simulating dislocation dissociation in FCC crystals, Acta Mater. 52 (2004) 683–691.
[27] C. Shen, J. Li, Y. Wang, Predicting structure and energy of dislocations and grain boundaries, Acta Mater. 74 (2014) 125–131.
[28] Y. Wang, J. Li, Phase field modeling of defects and deformation, Acta Mater. 58 (2010) 1212–1235.
[29] R. Peierls, The size of a dislocation, Proc. Phys. Soc. 52 (1940) 34.
[30] D. Qiu, P. Zhao, C. Shen, W. Lu, D. Zhang, M. Mrovec, Y. Wang, Predicting grain boundary structure and energy in BCC metals by integrated atomistic and phase-field modeling, Acta Mater. 164 (2019) 799–809.
[31] P. Zhao, T.S.E. Low, Y. Wang, S.R. Niezgoda, An integrated full-field model of concurrent plastic deformation and microstructure evolution: application to 3D simulation of dynamic recrystallization in polycrystalline copper, Int. J. Plast. 80 (2016) 38–55.
[32] P. Zhao, Y. Wang, S.R. Niezgoda, Microstructural and micromechanical evolution during dynamic recrystallization, Int. J. Plast. 100 (2018) 52–68.
[33] P. Zhao, C. Shen, S.R. Niezgoda, Y. Wang, Heterogeneous γ' microstructures in nickel-base superalloys and their influence on tensile and creep performance, Int. J. Plast. 109 (2018) 153–168.
[34] A.G. Khachaturyan, Theory of Structural Transformations in Solids, Courier Corporation, 2008.
[35] R.R. Zope, Y. Mishin, Interatomic potentials for atomistic simulations of the Ti-Al system, Phys. Rev. B 68 (2003), 024102.
[36] D. Qiu, R. Shi, P. Zhao, D. Zhang, W. Lu, Y. Wang, Effect of low-angle grain boundaries on morphology and variant selection of grain boundary allotriomorphs and widmanstätten side-plates, Acta Mater. 112 (2016) 347–360.
[37] D. Qiu, P. Zhao, R. Shi, Y. Wang, W. Lu, Effect of autocatalysis on variant selection of α precipitates during phase transformation in Ti-6Al-4V alloy, Comput. Mater. Sci. 124 (2016) 282–289.
[38] P. Partridge, The crystallography and deformation modes of hexagonal close-packed metals, Metall. Rev. 12 (1967) 169–194.
[39] D. Qiu, R. Shi, D. Zhang, W. Lu, Y. Wang, Variant selection by dislocations during α precipitation in α/β titanium alloys, Acta Mater. 88 (2015) 218–231.
[40] M. Mills, D. Hou, S. Suri, G. Viswanathan, Boundaries and Interfaces in Materials, vol 295, TMS, Warrendale, PA, 1998.
[41] R. Salloom, R. Banerjee, S. Srinivasan, Effect of β-stabilizer elements on stacking faults energies and ductility of α-titanium using first-principles calculations, J. Appl. Phys. 120 (2016) 175105.
[42] M.F. Savage, Microstructural and Mechanistic Study of Low Temperature Creep and Dwell Fatigue in Single Colony Alpha/Beta Titanium Alloys, Ph.D. thesis, The Ohio State University, 2000.
[43] J.R. Rice, Dislocation nucleation from a crack tip: an analysis based on the Peierls concept, J. Mech. Phys. Solids 40 (1992) 239–271.
[44] G. Xu, A.S. Argon, Homogeneous nucleation of dislocation loops under stress in perfect crystals, Phil. Mag. Lett. 80 (2000) 605–611.
[45] J.P. Hirth, J. Lothe, Theory of Dislocations, John Wiley & Sons, 1982.
[46] A.D. Crecy, A. Bourret, S. Naka, A. Lasalmonie, High resolution determination of the core structure of $1/3\langle11\overline{2}0\rangle\{10\overline{1}0\}$ edge dislocation in titanium, Philos. Mag. A 47 (1983) 245–254.
[47] S. Naka, A. Lasalmonie, P. Costa, L. Kubin, The low-temperature plastic deformation of α-titanium and the core structure of a-type screw dislocations, Philos. Mag. A 57 (1988) 717–740.
[48] J.S. Weaver, S.R. Kalidindi, Mechanical characterization of Ti-6Al-4V titanium alloy at multiple length scales using spherical indentation stress-strain measurements, Mater. Des. 111 (2016) 463–472.
[49] G. Lütjering, Influence of processing on microstructure and mechanical properties of $(\alpha+\beta)$ titanium alloys, Mater. Sci. Eng., A 243 (1998) 32–45.
[50] S. Raujol, M. Benyoucef, D. Locq, P. Caron, F. Pettinari, N. Clément, A. Coujou, Decorrelated movements of Shockley partial dislocations in the γ-phase channels of nickel-based superalloys at intermediate temperature, Phil. Mag. 86 (2006) 1189–1200.
[51] R.R. Unocic, N. Zhou, L. Kovarik, C. Shen, Y. Wang, M.J. Mills, Dislocation decorrelation and relationship to deformation microtwins during creep of a γ' precipitate strengthened Ni-based superalloy, Acta Mater. 59 (2011) 7325–7339.
[52] Z. Guo, A. Miodownik, N. Saunders, J.-P. Schillé, Influence of stacking-fault energy on high temperature creep of alpha titanium alloys, Scripta Mater. 54 (2006) 2175–2178.
[53] T. Zhu, J. Li, A. Samanta, H.G. Kim, S. Suresh, Interfacial plasticity governs strain rate sensitivity and ductility in nanostructured metals, Proc. Natl. Acad. Sci. 104 (2007) 3031–3036.